Exploiting Reaction-Diffusion Conditions to Trigger Pathway Complexity in the Growth of a MOF

Néstor Calvo Galve[+], Afshin Abrishamkar[+], Alessandro Sorrenti,* Lorenzo Di Rienzo, Mauro Satta, Marco D'Abramo,* Eugenio Coronado, Andrew J. de Mello, Guillermo Mínguez Espallargas,* and Josep Puigmartí-Luis*

Abstract: Coordination polymers (CPs), including metal–organic frameworks (MOFs), are crystalline materials with promising applications in electronics, magnetism, catalysis, and gas storage/separation. However, the mechanisms and pathways underlying their formation remain largely undisclosed. Herein, we demonstrate that diffusion-controlled mixing of reagents at the very early stages of the crystallization process (i.e., within ≈ 40 ms), achieved by using continuous-flow microfluidic devices, can be used to enable novel crystallization pathways of a prototypical spin-crossover MOF towards its thermodynamic product. In particular, two distinct and unprecedented nucleation-growth pathways were experimentally observed when crystallization was triggered under microfluidic mixing. Full-atom molecular dynamics simulations also confirm the occurrence of these two distinct pathways during crystal growth. In sharp contrast, a crystallization by particle attachment was observed under bulk (turbulent) mixing. These unprecedented results provide a sound basis for understanding the growth of CPs and open up new avenues for the engineering of porous materials by using out-of-equilibrium conditions.

Introduction

The self-organization of molecules into periodically ordered structures such as crystalline matter is of crucial importance in nature; for example, it has long been used for the evolution of living organisms.[1] However, the mechanisms and processes underlying the formation of crystalline materials remain still elusive and are largely undisclosed. Additionally, most of the efforts made to control crystallisation processes have relied so far on the adjustment of the molecular design as well as on the optimization of the experimental conditions used during the self-assembly processes (e.g. temperature, pH, ionic strength, and/or solvent composition). Remarkably, most of the crystallisation studies reported in the literature today are carried out under equilibrium conditions (i.e. thermodynamic control), which leads to thermodynamic products.[2] Nature, however, can master crystallisation processes and can obtain non-equilibrium crystal forms far from thermodynamic equilibrium by operating in out-of-equilibrium conditions.[1,3–7] Biomineralization, for instance, often occurs in the presence of chemical gradients, reaction-diffusion (RD) control, or hydrodynamic effects, which can lead to kinetic growth pathways.[1,6] Recently, the controlled diffusion of reagents through hydro-

[*] Dr. N. Calvo Galve,[+] Prof. E. Coronado, Prof. G. Mínguez Espallargas
Instituto de Ciencia Molecular (ICMol), Universidad de Valencia
C/ Catedrático José Beltrán, 2, 46980 Paterna (Spain)
E-mail: guillermo.minguez@uv.es

Dr. A. Abrishamkar,[+] Dr. A. Sorrenti, Prof. A. J. de Mello,
Prof. J. Puigmartí-Luis
Institute of Chemical and Bioengineering
Department of Chemistry and Applied Biosciences, ETH Zurich
8093 Zurich (Switzerland)
E-mail: asorrenti@ub.edu
josep.puigmarti@ub.edu

Dr. L. Di Rienzo
Fondazione Istituto Italiano di Tecnologia (IIT)
Center for Life Nano Science
Viale Regina Elena 291, I00161 Roma (Italy)

Dr. M. Satta
ISMN (CNR) c/o Department of Chemistry
Sapienza University of Rome
P.le Aldo Moro 5, 00185 Rome (Italy)

Prof. M. D'Abramo
Department of Chemistry, Sapienza University of Rome
P.le Aldo Moro 5, 00185 Rome (Italy)
E-mail: marco.dabramo@uniroma1.it

Dr. A. Sorrenti
Departament de Química Inorgànica i Orgànica (Secció de Química Orgànica) and Institut de Quimica Teorica i Computacional
Universitat de Barcelona
Martí i Franquès 1, 08028 Barcelona (Spain)

Prof. J. Puigmartí-Luis
Departament de Ciència dels Materials i Química Física and Institut de Quimica Teorica i Computacional
Universitat de Barcelona
Martí i Franquès 1, 08028 Barcelona (Spain)

Prof. J. Puigmartí-Luis
ICREA
Pg. Lluís Companys 23, 08010 Barcelona (Spain)

[+] These authors contributed equally to this work.

Supporting information and the ORCID identification number(s) for the author(s) of this article can be found under:
https://doi.org/10.1002/anie.202101611.

gel matrices has been exploited to modulate the habits of MOF crystals generated by periodic precipitation.[8] In addition, we reported on the formation of non-equilibrium shapes of peptide-based MOF single crystals obtained by confined crystallization within microchambers that mimic microgravity conditions.[9] Yet, the effect of fluid flow phenomena in self-assembly processes have been largely overlooked in chemistry and materials science.[10–12] Accordingly, there is a pressing need to control the fluid dynamic behaviour of reagents as well as their reaction-diffusion area in artificial systems. Likewise, in nature, non-equilibrium experimental conditions can aid not only to elucidate the pathway complexity underlying the formation of complex self-assembled materials, but more importantly, to control the hiking of crystalline matter on the free energy landscape during the self-assembly process. Such a control, despite being very well pictured in nature, still remains elusive with conventional synthetic methods.[13,14]

Herein, we demonstrate that liquid-liquid interfacial reactions occurring in continuous-flow microfluidic devices and operating at the very early stages of the crystallization process can steer the following off-chip crystal growth towards novel growth pathways along a fixed energy landscape (i.e., while keeping constant the final experimental conditions). Those kinetic growth pathways, which are triggered over a millisecond timescale by a controlled space-time strategy (controlled RD), can neither be observed nor generated by conventional bulk (flask) mixing (e.g., by common temperature/time dependent synthetic protocols).[14,15]

Note that the vast majority of crystallization studies conducted with microfluidic technologies usually focus on the use of microfluidic devices as convenient analytical tools for monitoring crystal growth and extracting parameters related with the crystal growth kinetics, (e.g. by integrating in situ detection systems), or instead, microfluidic devices are simply employed as high throughput screening platforms for fast data collection and optimization of crystallization conditions.[16–19] However, the laminar flow conditions that are characteristic of most microfluidic systems, where mixing of reagents only occurs through molecular diffusion,[14,20] may enable unprecedented control over crystallization processes in space (i.e. the nucleation and/or crystal growth only occurs in the RD area generated between the co-flowing reagent streams) and time (the reaction proceeds along the length of the microfluidic channel).[14] Additionally, and in contrast to bulk synthetic approaches, microfluidic liquid-liquid interfacial reactions are characterized by a constant mass transport of reagent species to the RD area. This last condition has been advantageously used, for instance, to isolate early states of crystallization along a single kinetic pathway.[21] Here, and in sharp contrast to previous work with laminar flows, we show how continuous-flow microfluidic devices, used to control reagents mixing at the very early stages of the crystallization process, can unveil and enable different kinetic pathways in the growth of the same crystalline material (Figure 1). Our approach yields important mechanistic insights into the formation of a prototypical multifunctional CP while providing the first clear example of pathway complexity in the field.

Namely, inspired by recent research showing multifunctionality in CPs, we studied the crystallization process of **CCP-4**[22] (standing from Compartmentalized Coordination Polymer), a magnetically active MOF with a general formula [Fe-(btzbp)$_3$](BF$_4$)$_2$ (where btzbp stands for 4,4′-bis((1H-tetrazol-1-yl)methyl)-1,1′-biphenyl).[23]

Results and Discussion

In a previous study, we prepared **CCP-4** in bulk conditions by mixing btzbp and Fe(BF$_4$)$_2$·6H$_2$O in acetonitrile under turbulent stirring conditions protracted for a few days (i.e., under thermodynamic control).[22] **CCP-4** was obtained as a white microcrystalline powder constituted by perfectly hexagonal crystals, whose structure was solved by single crystal X-ray diffraction at two different temperatures (refcodes QACVOI and QACVOI01). Importantly, the crystal habit could be directly related to the hexagonal symmetry of **CCP-4** crystal structure, which belongs to the space group $P6_3$. In this preliminary study, the attention was focused on the changes of the magnetic properties of the equilibrium crystals in response to an external stimulus, such as CO_2 adsorption, but not on the mechanisms and pathways underlying **CCP-4** crystal growth. Herein, we use a continuous-flow microfluidic device comprising four inlets and one outlet to achieve kinetic control during the assembly of **CCP-4** crystals (see Figure 1B and Supporting Information). Such a microfluidic configuration allows to establish a controlled RD area within the main microfluidic channel (purple area in Figure 1C), because of the laminar flow regime present in the device.[14] In a typical experiment, acetonitrile solutions of Fe(BF$_4$)$_2$·6H$_2$O (15.7 mM) and btzbp (31.4 mM) were separately injected into the two middle input channels (b and c in Figure 1C), while two pure acetonitrile sheath flows were introduced from inlets a and d (Figure 1C). The flow rate ratio (FRR)—i.e., the ratio between the flow rates of the reagent-laden flows and that of the sheath flows- was fixed to 1, and the evolution of the structures generated under microfluidic conditions, hereafter referred to as **MF-CCP-4**, were studied over time by transmission electron microscopy (TEM) (further details in Supporting Information).

Specifically, the solution eluting from the microfluidic device was collected in a vial and analysed offline at different time intervals (i.e. 1, 3, 6, 12 and 24 hours) by TEM (vide infra). In addition, to analyse **MF-CCP-4** samples at time zero, that is, just downstream the microfluidic channel, the solution exiting the outlet was immediately drop-cast onto a TEM grid using a blotting method, which ensures a rapid quenching of the reaction as previously reported.[24] Interestingly, the TEM analysis of those time-zero **MF-CCP-4** samples revealed the presence of particle-like aggregates with sizes ranging between 200 nm and 600 nm (Supporting Information, Figure S1). Attempts to characterize these particles by selected area electron diffraction (SAED) failed, since they were promptly damaged even after short electron beam irradiation. Nevertheless, energy dispersive X-ray (EDX) measurements indicated the presence of both N and Fe in the particles, confirming that they comprise both
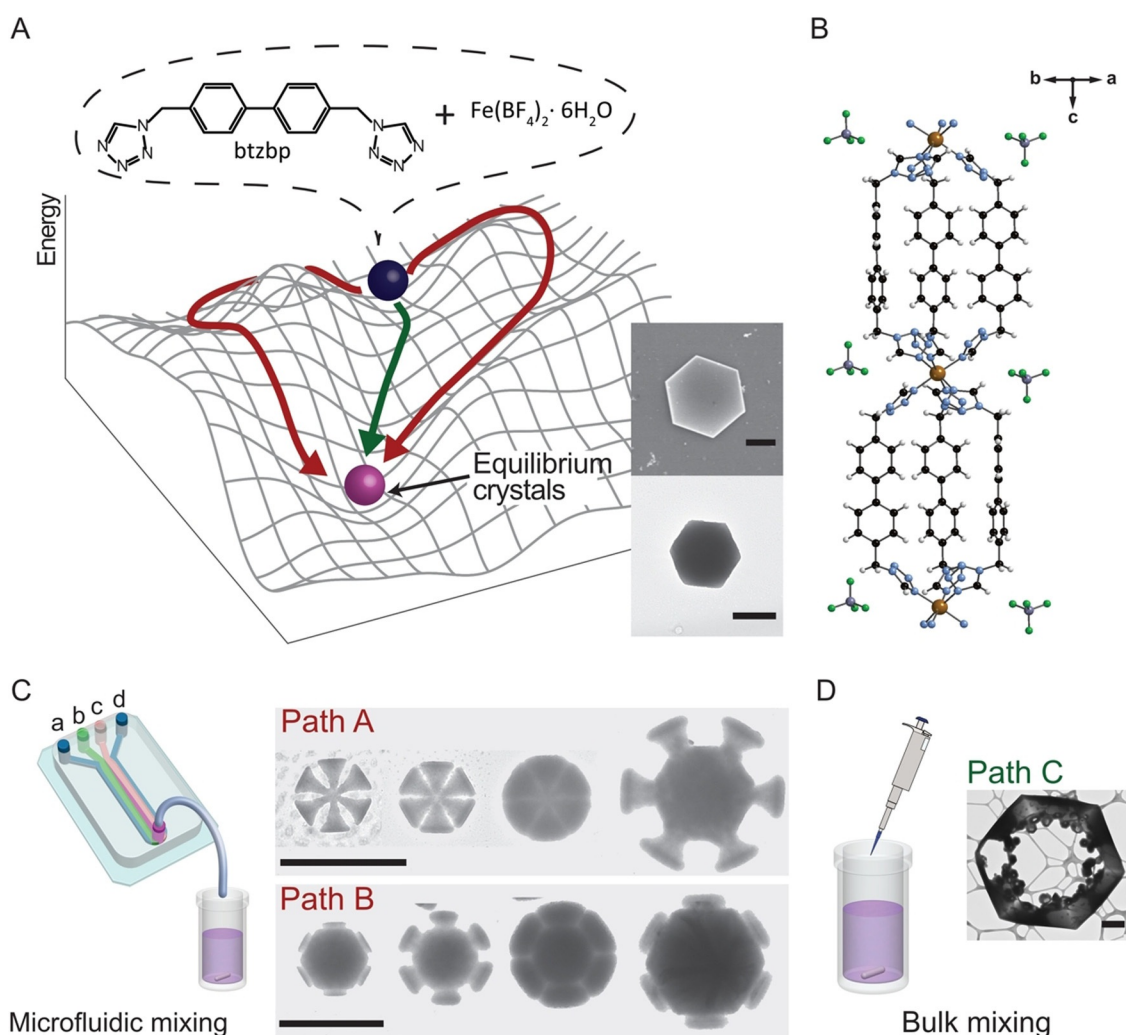
Figure 1. Selection of different crystallization pathways depending on the mixing protocol. A) Schematic illustration of kinetic (red) and thermodynamic (green) pathways followed by the system towards the thermodynamic product (i.e. equilibrium hexagonal crystals). Representative SEM and TEM images of the thermodynamic product as observed 24 h after the synthesis, as well as the chemical structure of the ligand btzbp are also presented. B) Structure of the CP chain along the *c* axis (only three Fe atoms are reported). C) Schematic illustration of the RD area generated within the continuous flow microfluidic device (pink colour), and representative TEM images showing the sequential growth along the two kinetic pathways: *Path A* (vertex growth) and *Path B* (edge growth). The intermediates ascribable to *Path A* (top row) are mainly observed between 1 and 6 hours of reaction, whereas the intermediates belonging to *Path B* (bottom row) are mainly observed between 6 and 12 hours of reaction. D) Representative TEM image of the kind of intermediates observed in the samples prepared by bulk mixing after 1 h of reaction. Note that the samples prepared by microfluidic and bulk mixing were obtained under identical final experimental conditions, i.e., same concentration of btzbp (8.0 mM) and $Fe(BF_4)_2 \cdot 6 H_2O$ (4.0 mM), same temperature (room temperature) and solvent composition. Scale bars: 2 µm in (A), 4 µm in (C) and 1 µm in (D).

reagent precursors (Supporting Information, Figure S2). In marked contrast, **CCP-4** samples synthesized in bulk (under magnetic turbulent stirring) did not show any reaction product at time zero (i.e. when drop-cast on TEM grids soon after the mixing of the reagents). The latter result is significant, considering that we used the same precursor solutions for the synthesis of both bulk and microfluidic (time-zero) samples.

When we analysed the time evolution of the microfluidic product **MF-CCP-4** by time-course TEM analysis, we could clearly identify two different pathways in the growth of **MF-CCP-4** crystals, which we refer to as *Path A* and *Path B* (Figure 1 C). Specifically, in *Path A*, the crystal growth

proceeds from the vertices of a previously formed **MF-CCP-4** structure (vertex growth), while in *Path B* the growth proceeds from the edges of hexagonally shaped **MF-CCP-4** aggregates (edge growth). The careful analysis of TEM images collected at different time points clearly confirmed that the two crystallization pathways involve distinct intermediates, thus representing two competing routes undertaken simultaneously by the system along the free energy landscape (Figure 1 A and C). In particular, we found out that *Path A* and *Path B* differ with regard to the relative orientation of the growing particles. In fact, while the vertex growth through *Path A* implies a 30° rotation of the hexagonal intermediates at each growth step (Figure 2 A), the edge growth along *Path*
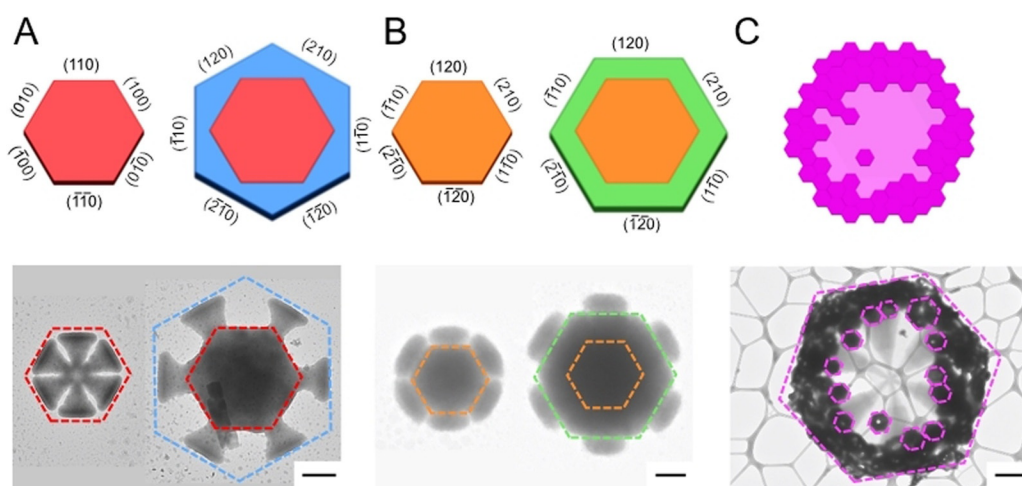
Figure 2. Schematic illustration and representative TEM images of the crystal growth along the different pathways. A) Vertex growth (*Path A*) with a 30° rotation of the orientation hexagonal intermediates at each growth step, B) edge growth (*Path B*), and C) crystallization by particle attachment (*Path C*). (A) and (B) are **MF-CCP4** samples and (C) is the intermediate state found as a result of the bulk synthesis. Scale bars are 1 μm.

B preserves the orientation of the growing intermediates (Figure 2B). Thus, whereas *Path A* involves a change of the crystallographic faces of the hexagonal crystal with each growth step, Path B retains the same faces. In fact, re-examination of the diffraction data of the two reported crystals allows the identification of two different face indexing of the hexagonal morphology, otherwise indistinguishable to the eye. Thus, the observed faces in one crystal are the (100), (010) and (110), and symmetry related, whereas in the other crystal the observed faces are $(\bar{1}10)$, (210) and (120) and symmetry related (see Figure 2).

Remarkably, however, both *Path A* and *Path B* ultimately yield indistinguishable hexagonal crystallites 24 hours after collection, which are identical to the bulk synthesized **CCP-4** crystals in terms of morphology (Supporting Information, Figure S3), X-ray powder diffraction pattern (Supporting Information, Figure S4) and SCO magnetic behaviour (Supporting Information, Figure S5). That is, *Path A* and *Path B* eventually lead to the thermodynamically stable **CCP-4** crystal form, despite being two distinct hiking routes across the free energy landscape of the system, which involve a series of different intermediates (Figure 1 A and C). We point out that the unprecedented intermediate morphologies observed along the offline growth of **MF-CCP-4** crystals arise and evolve from nucleation events that occur under controlled RD conditions operating for a period as short as 40 ms, which is the residence time of the reagent solutions in the main microfluidic channel. It should also be noted that changes in the total flow rate (TFR) do not change the general outcome, but simply the number of structures generated, while increasing the FRR prevents the reaction, with no **MF-CCP-4** aggregates observed by TEM imaging (further details in Supporting Information).

In light of the results obtained for **MF-CCP-4** samples, we studied in more detail the growth of bulk synthesized **CCP-4** crystals by time-course TEM analysis, aimed at uncovering possible differences in the growth pathways undertaken by

the system under controlled RD conditions (microfluidic mixing) versus equilibrium conditions (turbulent bulk mixing). Accordingly, we prepared **CCP-4** samples for TEM analysis by directly drop casting the reaction solution on TEM grids at the same time intervals as those investigated for microfluidic samples. Surprisingly, and in sharp contrast to what was observed for **MF-CCP-4** samples, the TEM images of 1 h aged **CCP-4** samples revealed the presence of incomplete crystals with a hexagonal morphology, which appear to be formed by the assembly of smaller hexagonal crystallites (Figure 1 D and Supporting Information, Figures S6 and S7). Moreover, all TEM samples prepared from bulk solutions aged for 3 h or longer resulted in empty TEM grids. In fact, we observed that **CCP-4** crystals completely precipitate out of the reaction mixture already 3 h after preparation, leaving a clear supernatant solution. SEM images of the precipitate confirmed the presence of fully grown **CCP-4** crystals with hexagonal shape (Figure 1 A and Supporting Information, Figure S8). These results clearly demonstrate that **CCP-4** crystals grow by following a different pathway along the free energy landscape that we refer to as *Path C* (Figure 1 A and 2 C). In *Path C*, which is selected under thermodynamic control, the growth process of **CCP-4** crystals proceeds through the attachment of hexagonal particles that maintain the same orientation as the final crystals (Figure 2 C). In addition, *Path C* overall results in faster crystallization with complete precipitation of the product within 3 hours. To the best of our knowledge, this is the first example of mesoscale assembly in a SCO MOF where the final superstructures, which are in fact single crystals as previously reported, are clearly assembled from colloidal intermediates via an oriented aggregation process, yielding crystals with low mosaicity (ca. 1–2°).[7,25] It is important to remark that: i) **CCP-4** and **MF-CCP-4** samples were prepared under identical final experimental conditions (i.e. room temperature, final concentration of btzbp (8.0 mM) and Fe-$(BF_4)_2 \cdot 6H_2O$ (4.0 mM), and solvent composition); ii) both

microfluidic and bulk mixing lead eventually to indistinguishable hexagonal crystals that correspond to the thermodynamic product (Figure 1 A and compare Supporting Information, Figures S3 and S8). Nevertheless, kinetic control under microfluidic conditions steers the system along two nucleation-growth pathways characterized by well-defined metastable intermediates (*Path A* and *Path B*), which have never been observed under bulk conditions. On the other hand, under thermodynamic control (bulk mixing) the crystallization proceeds through a particle attachment mechanism (*Path C*), also known as mesoscale assembly.[7] This is a clear and remarkable example of pathway selection in a crystallization process. Once kinetic pathways (*Path A* or *Path B*) are selected under controlled RD conditions, the system is forced to follow them "downhill" towards the final product and cannot go "uphill" to follow the fastest thermodynamic pathway, that is, *Path C* (red and green lines in Figure 1 A respectively).

We stress that our system is different from the cases in which a change of the crystallization mechanism or even of the outcome of the crystallization process (e.g. in terms of phase or morphology of the generated crystals) are accomplished by changing parameters such as supersaturation,[7] solvent composition[26] or temperature. In fact, in such cases the shape of the free-energy landscape and consequently of the energy barriers change due to the change of the experimental conditions. On the other hand, we present here a true example of pathway selection in a hierarchical self-assembly process in which the energy landscape of system is fixed by the final experimental conditions (we used the same conditions for bulk and microfluidic synthesis), but the system can be steered to follow different hiking routes towards the final thermodynamic product depending on the preparation

procedure (i.e., controlled diffusion of reagents vs. turbulent mixing).[13]

Competition between *Path A* and *Path B*. We subsequently studied in more detail the competition between the two nucleation-and-growth crystallization pathways (*Path A* and *Path B*) observed upon microfluidic mixing both by experiments and by full-atom molecular dynamics (MD) simulations. A statistical analysis of the abundance of each type of intermediate at given time intervals indicates that the vertex growth (*Path A*) is kinetically favoured (faster) with respect to edge growth (*Path B*). Specifically, the analysis of > 850 microcrystals from TEM images showed that 94% of the **MF-CCP4** particles observed in 1 h aged samples feature a vertex-based growth (i.e. belong to *Path A*). On the other hand, **MF-CCP-4** particles featuring edge growth (i.e. belonging to *Path B*) become predominant only in samples aged 6 h or longer (Supporting Information, Figures S9 to S13 and Table S1). Since the microfluidic synthesis ultimately yields a product indistinguishable from the bulk prepared one, the growth through *Path A* and *Path B*, and the kinetic preference for the former, can be rationalized in terms of the supramolecular interactions present in the crystal structure solved for **CCP-4**.[7] Figure 3 shows the crystal faces of the hexagonal crystals, with the *a* and *b* axes oriented with respect to the observed morphology of the crystals, as experimentally indexed. The sections of the crystal perpendicular to the *c* axis (i.e. perpendicular to the (001) plane) indicate that the corners of the hexagons correspond to the position where BF_4^- counter-ions (shown in yellow in Figure 3 B and C) accumulate, whereas the edges of the hexagons correspond to the position of the biphenyl moiety of the organic ligands (yellow moieties in Figure 3 E and F). Accordingly, the growth through *Path A* is likely to be driven by electrostatic interactions involving BF_4^- anions, whereas the growth along
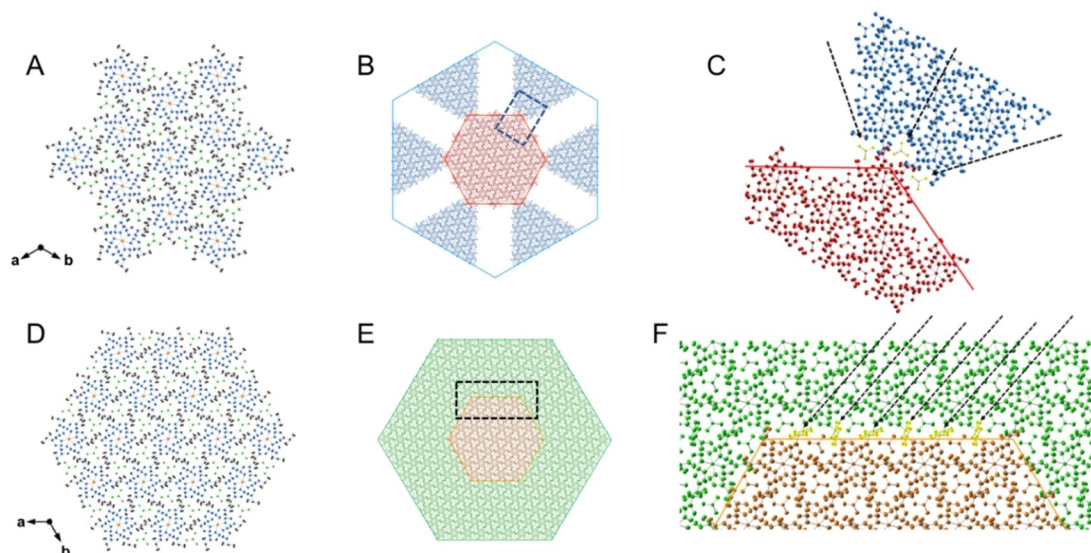

Figure 3. Crystal structure of **CCP-4**. (A) corresponds to a cluster of formula ${[Fe(btzbp)_3]_{13}(BF_4)_{24}}^{2+}$ and (D) to a cluster of formula ${[Fe(btzbp)_3]_{19}(BF_4)_{36}}^{2+}$. (B) and (E) are illustrations of putative **MF-CCP-4** intermediate structures built employing the indexed crystal structure of **CCP-4**. C) A detail of the vertex region of a hexagonal cluster where the growth through *Path A* is expected to be dominated by electrostatic interaction involving negative BF_4^- anions (depicted in yellow). F) The edge region of a hexagonal cluster is shown where the growth through *Path B* is expected to be driven by π–π interactions due to the presence of the phenyl groups of the organic ligands (shown in yellow).

Path B should mostly involve weaker π-π interactions. The different driving force would also account for the faster growth through *Path A*, since Coulombic interactions are known to be energetically more relevant than van der Waals forces in crystallization processes.[7] It is important to stress that the coordination interactions between Fe nuclei and the organic linker btzbp run along the *c* axis, that is, perpendicularly to the cross-sections along the *ab* plane depicted in Figure 3. In other words, the CP's backbone of formula $[\mathrm{Fe}_n(\mathrm{btzbp})_{3n}]^{2n+}$ is a one-dimensional chain that runs parallel to the *c* axis (Figure 1 B and Supporting Information, Figure S14), while the growth of the hexagonal crystallites in the *ab* plane (according to *Path A* and *Path B*) corresponds to a supramolecular polymerization where single CP strands, formed within the microfluidic chip, bind to a preformed

hexagonal cluster via electrostatic and van der Waals interactions (Supporting Information, Figure S14).

To shed further light on the competition between the two growth pathways, *Path A* and *Path B*, we performed all-atom MD simulations in acetonitrile solvent. In order to simulate the nucleated supramolecular polymerization, we first build up a cluster made of nineteen strands of the coordination polymer—each with formula $[\mathrm{Fe}_3(\mathrm{btzbp})_9](\mathrm{BF}_4)_6$ (Supporting Information, Figure S15)—disposed according to the hexagonal close-packed crystal structure of **CCP-4**, as shown in Figure 4 A (see Supporting Information for further details). The analysis of the root-mean-square-distance (RMSD) reveals that the cluster is stable and does not disassemble during the 1 μs long MD simulation. In particular, after an initial equilibration period (≈ 100 ns), the RMSD reaches
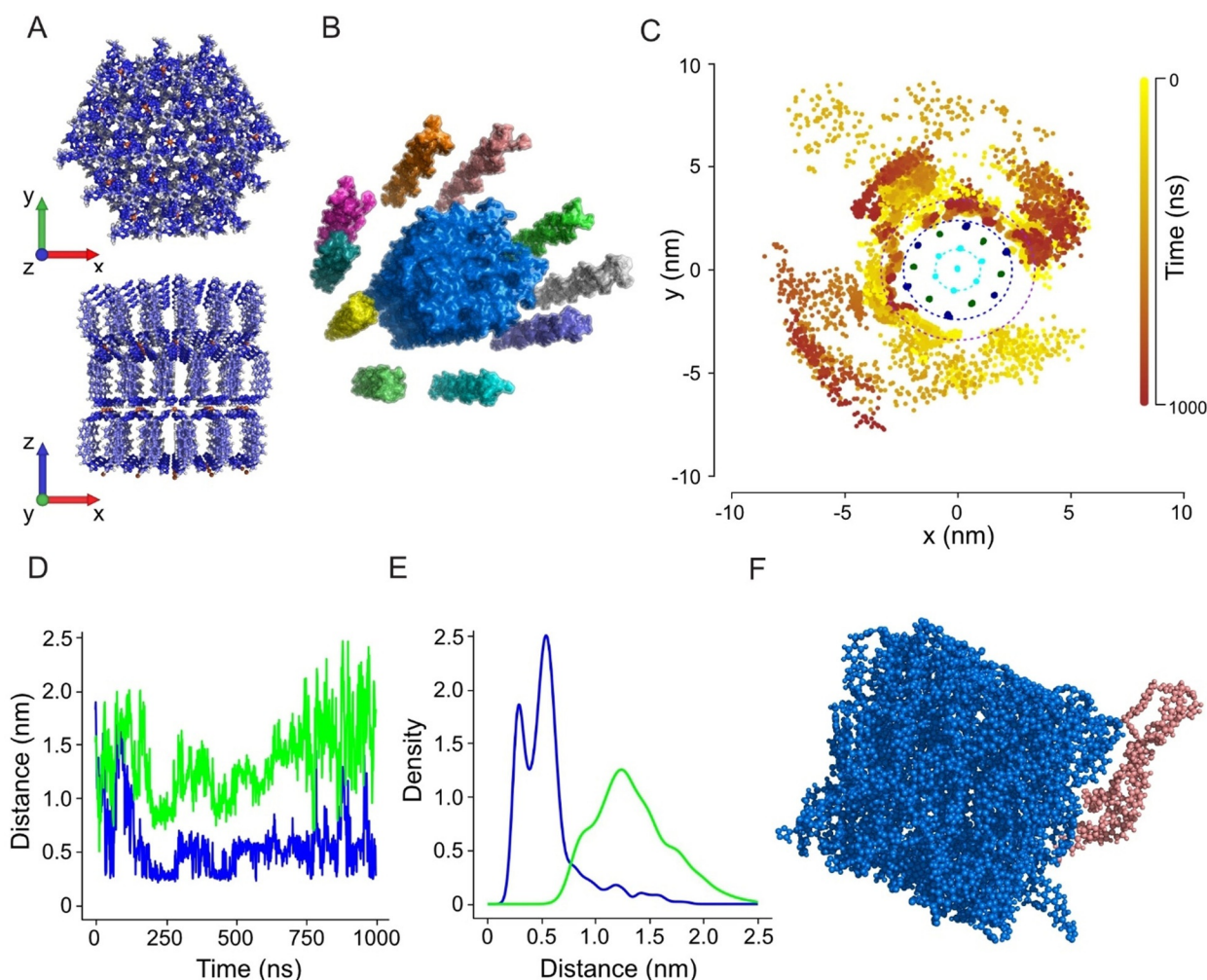

Figure 4. Results from the MD simulations. A) Initial configuration of the cluster formed by nineteen CP strands with formula $[\mathrm{Fe}_3(\mathrm{btzbp})_9](\mathrm{BF}_4)_6$ disposed accordingly to the crystal structure reported in Figure 3 D (top and lateral view are reported). The formula of the cluster is therefore $[\mathrm{Fe}(\mathrm{btzbp})_3]_{57}(\mathrm{BF}_4)_{104}$. B) Initial configuration of the MD simulation comprising the central cluster and additional ten CP strands placed at random positions (and at a distance greater than 1 nm) around it. C) MD trajectories of the ten strands in the *xy* plane represented by tracking the position of the atom of each strand closest to the central cluster. The position of the free strands is coloured according to their time evolution using a yellow-orange look up table. The nineteen strands forming the central cluster are represented as filled dots of different colours depending on their position in the cluster, cyan, blue and green for inner, vertex and edge units, respectively (see also Supplementary Figure 17). The dotted circles are drawn as a guide for the eyes. The outer one (purple) has a radius 1 nm larger than the inner one (blue). D) Time evolution of the strand-to-vertex (blue) and strand-to-edge (green) distances of one of the ten free strands taken as an example. E) Density distributions of the distances reported in (D). F) A snapshot of the MD simulation showing a configuration where a free strand is interacting with the vertex region of the cluster.

a plateau with the overall geometrical parameters and atomic motions showing very limited deviations from the initial structure, in line with the expected behaviour of rigid crystalline systems (Supporting Information, Figure S16 and Supporting Information, Table S2). This makes us confident that a description of the early steps of the crystal growth from a preformed nucleus can be attempted by our theoretical-computational procedure.

To this aim, we performed a further MD simulation (1 µs) starting from a configuration in which ten additional CP strands are placed at random positions around the equilibrated hexagonal cluster and at a distance greater than 1 nm from the central unit, that is, far enough to prevent any bias due to the position with respect to the central cluster (Figure 4B and Supporting Information, Figure S17). The interaction between the free strands and the central cluster was characterised by monitoring the trajectories of the ten strands and calculating the strand-to-cluster distances along them. Figure 4C shows the MD trajectories of the ten strands represented by tracking the position of the atom of each strand that is closest to the central cluster (see Supporting Information). The data collected clearly indicate that: i) the strands have the possibility to explore the entire space around the cluster; ii) the strands spend a remarkable fraction of their trajectories ($\approx 80\%$) at a distance shorter than 1 nm from the cluster, that is, in interaction with it (purple dashed circle in Figure 4C); iii) the cluster does not disassemble during the diffusion of the strands.

To extract further information from the MD simulation and to connect this information with the growth pathways observed experimentally, we analysed the interaction between the strands and the central cluster from a more geometrical point of view. In particular, we first classified the nineteen strands that make up the cluster as internal, vertex or edge units (cyan, blue and green dots, respectively in Figure 4C and Supporting Information, Figure S18). Then for each of the ten free strands we calculated the time evolution of its distance to both the nearest vertex and edge units of the cluster (Supporting Information, Figure S19). From such an analysis, a clear pattern emerged. Namely, considering a cut-off of 1 nm (slight variations of the cut-off do not affect the result), the free strands approach the central cluster from its vertex in 9 out of 10 cases (Supporting Information, Figure S18). In other words, when in the interaction region (i.e. at less than 1 nm from the cluster), the free strands spend more time closer to a vertex unit than to an edge unit of the cluster (Supporting Information, Figures S19–21). Panels D and E in Figure 4 show the time evolution of the strand-to-vertex (blue line) and strand-to-edge (green line) distances for an exemplary strand as well as the density distributions corresponding to those distances, respectively. To sum up, although the time scale of the simulations is limited with respect to the experimental one, MD data clearly shows that at the early stages of the crystal growth there is a preference for the binding to the vertices of the cluster, which supports the experimental observation that *Path A* is kinetically favoured. One representative configuration of the system in which a free strand is interacting with the vertex region of the cluster is shown in Figure 4F.

Conclusion

In light of the results presented, it is clear that the controlled reaction-diffusion conditions present in our microfluidic devices provide access to new crystallization pathways characterized by unprecedented intermediate species, which are not observed under bulk thermodynamic conditions. We believe that the continuous but controlled supply of reagents in the RD region favours the formation of strands of the coordination polymer (i.e. driven by stronger coordination interaction), and this allows to exert more control over the nucleated supramolecular polymerization at the base of the crystal growth in *Path A* and *Path B.* In particular, during the microfluidic synthesis small particles of **MF-CCP-4** are formed (clusters of strands), which evidently coexist with free CP strands (or even with unreacted metal and ligand precursors) likely due to incomplete mixing during the residence time in the chip (milliseconds).[21,27] These particles once formed in the microfluidic environment act as nuclei in the following classical (monomer-to-cluster) crystal growth that occur over several hours offline. MD simulation confirmed that small clusters of CP strands are, in fact, stable (do not disassemble) and can bind other strands in their outer surface. In addition, the MD data also confirmed that the vertex growth is favoured (faster) than the lateral growth. In sharp contrast, bulk mixing results in the homogeneous formation of a high number of micrometre-sized hexagonal crystallites with depletion of free CP strands (i.e. many nuclei form once the barriers to nucleation is overcome and grow rapidly to the micrometre size consuming CP strands). As a result, further crystal growth can only occur by a particle attachment mechanism.[7]

Our investigations demonstrate that continuous-flow microfluidic devices will play an extremely important role for studying crystallization processes and unveiling their pathway complexity, as well as for potentially achieve pathway selection. In the field of functional self-assembled materials, it is crucial to study and understand the mechanism of formation of ordered supramolecular structures. For example, the systematic manipulation of the growth of functional crystals can result in controllable structures with defined properties. To date, however, purely thermodynamic approaches have had limited success in this material challenge. For these reasons, we believe that our method will potentially open new horizons not only in future CP and MOF research, but also in the quest to engineer novel functional materials.

Acknowledgements

[1] S. Mann, *Biomineralization: Principles and Concepts in Bioinorganic Materials Chemistry*, Oxford University Press, Oxford, **2001**.

[2] N. Stock, S. Biswas, *Chem. Rev.* **2012**, *112*, 933 – 969.

[3] L. Addadi, S. Weiner, *Angew. Chem. Int. Ed. Engl.* **1992**, *31*, 153 – 169; *Angew. Chem.* **1992**, *104*, 159 – 176.

[4] L. Addadi, A. Gal, D. Faivre, A. Scheffel, S. Weiner, *Isr. J. Chem.* **2016**, *56*, 227 – 241.

[5] F. Nudelman, N. A. J. M. Sommerdijk, *Angew. Chem. Int. Ed.* **2012**, *51*, 6582 – 6596; *Angew. Chem.* **2012**, *124*, 6686 – 6700.

[6] S. Weiner, L. Addadi, *Annu. Rev. Mater. Sci.* **2011**, *41*, 21 – 40.

[7] J. J. De Yoreo, P. U. P. A. Gilbert, N. A. J. M. Sommerdijk, R. L. Penn, S. Whitelam, D. Joester, H. Zhang, J. D. Rimer, A. Navrotsky, J. F. Banfield, A. F. Wallace, F. M. Michel, F. C. Meldrum, H. Cölfen, P. M. Dove, *Science* **2015**, *349*, aaa6760.

[8] J. H. Park, J. Paczesny, N. Kim, B. A. Grzybowski, *Angew. Chem. Int. Ed.* **2020**, *59*, 10301 – 10305; *Angew. Chem.* **2020**, *132*, 10387 – 10391.

[9] A. Sorrenti, L. Jones, S. Sevim, X. Cao, A. J. deMello, C. Martí-Gastaldo, J. Puigmartí-Luis, *J. Am. Chem. Soc.* **2020**, *142*, 9372 – 9381.

[10] J. M. Ribó, J. Crusats, F. Sagués, J. Claret, R. Rubires, *Science* **2001**, *292*, 2063 – 2066.

[11] A. Sorrenti, Z. El-Hachemi, J. Crusats, J. M. Ribo, *Chem. Commun.* **2011**, *47*, 8551 – 8553.

[12] J.-K. Sun, Y. I. Sobolev, W. Zhang, Q. Zhuang, B. A. Grzybowski, *Nature* **2020**, *579*, 73 – 79.

[13] A. Sorrenti, J. Leira-Iglesias, A. J. Markvoort, T. F. A. de Greef, T. M. Hermans, *Chem. Soc. Rev.* **2017**, *46*, 5476 – 5490.

[14] S. Sevim, A. Sorrenti, C. Franco, S. Furukawa, S. Pané, A. J. deMello, J. Puigmartí-Luis, *Chem. Soc. Rev.* **2018**, *47*, 3788 – 3803.

[15] M. Lu, A. Ozcelik, C. L. Grigsby, Y. Zhao, F. Guo, K. W. Leong, T. J. Huang, *Nano Today* **2016**, *11*, 778 – 792.

[16] J. Leng, J.-B. Salmon, *Lab Chip* **2009**, *9*, 24 – 34.

[17] M. Sultana, K. F. Jensen, *Cryst. Growth Des.* **2012**, *12*, 6260 – 6266.

[18] S. Zhang, C. J. J. Gerard, A. Ikni, G. Ferry, L. M. Vuillard, J. A. Boutin, N. Ferte, R. Grossier, N. Candoni, S. Veesler, *J. Cryst. Growth* **2017**, *472*, 18 – 28.

[19] I. Lignos, R. Maceiczyk, A. J. deMello, *Acc. Chem. Res.* **2017**, *50*, 1248 – 1257.

[20] K. S. Elvira, X. C. i Solvas, R. C. R. Wootton, A. J. deMello, *Nat. Chem.* **2013**, *5*, 905.

[21] M. Rubio-Martinez, I. Imaz, N. Domingo, A. Abrishamkar, T. S. Mayor, R. M. Rossi, C. Carbonell, A. J. deMello, D. B. Amabilino, D. Maspoch, *Adv. Mater.* **2016**, *28*, 8150 – 8155.

[22] N. Calvo Galve, M. Giménez-Marqués, M. Palomino, S. Valencia, F. Rey, G. Mínguez Espallargas, E. Coronado, *Inorg. Chem. Front.* **2016**, *3*, 808 – 813.

[23] G. Mínguez Espallargas, E. Coronado, *Chem. Soc. Rev.* **2018**, *47*, 533 – 557.

[24] J. Puigmartí-Luis, D. Schaffhauser, B. R. Burg, P. S. Dittrich, *Adv. Mater.* **2010**, *22*, 2255 – 2259.

[25] A.-W. Xu, M. Antonietti, H. Cölfen, Y.-P. Fang, *Adv. Funct. Mater.* **2006**, *16*, 903 – 908.

[26] A. Bacchi, G. Cantoni, D. Cremona, P. Pelagatti, F. Ugozzoli, *Angew. Chem. Int. Ed.* **2011**, *50*, 3198 – 3201; *Angew. Chem.* **2011**, *123*, 3256 – 3259.

[27] A. Sorrenti, R. Rodriguez-Trujillo, D. B. Amabilino, J. Puigmartí-Luis, *J. Am. Chem. Soc.* **2016**, *138*, 6920 – 6923.